Inorganic Chemistry Communications 146 (2022) 110198

Contents lists available at ScienceDirect

Inorganic Chemistry Communications

journal homepage: www.elsevier.com/locate/inoche

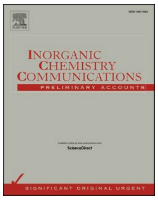

Synthesis, crystal structure, DFT calculations, Hirshfeld surface analysis and molecular docking studies of a new manganese complex

Ali Akram Derardja [a,b], Lynda Golea [a,c], Rim Benali-Cherif [a,c,*], Dominique Luneau [d], Zina Boutobba [a,c], Youcef Boumedjane [e], Hassina Harkat [f]

[a] *Department of Material Sciences, Faculty of Science and Technology, Abbes Laghrour-Khenchela University, Khenchela 40000, Algeria*
[b] *Laboratory of Advanced Materials Engineering and Sciences (ISMA), Abbes Laghrour-Khenchela University, Khenchela 40000, Algeria*
[c] *Laboratoire des Structures, Propriétés et Interactions Inter Atomiques (LASPI2A), Abbes Lagrour-Khenchela University, Khenchela 40000 Algeria*
[d] *Université Claude Bernard Lyon 1, Laboratoire des Multimatériaux et Interfaces (UMR 5615), Campus de La Doua, 69622 Villeurbanne Cedex, France*
[e] *Laboratory of Molecular Chemistry and Environment (LCME), Faculty of Sciences and Exact Sciences, Department of Material Sciences, University of Biskra, BP 145 RP, 07000 Biskra, Algeria*
[f] *Laboratory of Physio-toxicology, Cellular and Molecular-biomolecular Pathology (LPTPCMB), Faculty of Medicine, Department of Pharmacy, University of Batna-2, Batna, Algeria*

ARTICLE INFO

Keywords:
Schiff base
Manganese complex
Aromatic stacking interactions
Supramolecular synthons
Molecular docking
DFT calculations

ABSTRACT

Mn^{II}-based coordination compound $[Mn^{II}(L)_2(NO_3)(H_2O)_3]NO_3$ **(3)** has been synthesized with Shiff's base N^2-benzylidenyl isonicotinic acid hydrazide **(2)** and ($Mn(NO_3)_2{\cdot}4H_2O$). The compound is new and has been fully characterized by FT-IR, UV–visible, 1H and ^{13}C NMR spectroscopic techniques and single-crystal X-ray diffraction complemented with a quantum chemical study performed with DFT method. The compound crystallized in the monoclinic centrosymmetric $P2_1/n$ space group. The crystal structure of **(3)** exhibits a nitrate anion and a non-centrosymmetric complex cation $[Mn^{II}(L)_2(NO_3)(H_2O)_3]^+$. In the molecular packing, the different entities are held together through intermolecular strong, weak and non-conventional O/N/C—H···O hydrogen bonds, that found to be effective in stabilizing the three-dimensional network. Furthermore, the crystal structure of (**3**) contains interesting cyclic supramolecular homo and heterosynthons. Moreover, π–π stacking and $N_{lone\text{-}pair}\cdots$C—H intermolecular electrostatic interactions play a crucial role in building a supramolecular layered network.

To better understand the contribution of different intermolecular interactions to the supramolecular assembly, Hirshfeld surface analysis was performed. The obtained results indicate that the main contributions are attributed to O—H···O, N—H···O and C—H···O interactions which are the primary giver the stabilisation in the crystal. The theoretical achievements were found in a good relation with the experimental structural analysis. The HOMO and LUMO energies and molecular electrostatic potential surface were derived from the same basis and the natural population Mulliken charge distribution analysis showed the different electron donors which coordinate with manganese. In addition to that, the molecular docking for **(2)** and **(3)** investigation with the 2X22 enzyme involved in Mycobacterium tuberculosis H37Rv have been conducted in order to check the biological activity of the Schiff base and its complex.

1. Introduction

The azomethine group (—RC=N—) or imines, are often called Schiff's bases after the work of the German chemist Hugo Schiff who developed this new class of organic compounds late 19th century. Most generally, the imine function result from the condensation reaction of a primary amine with an active carbonyl compound. Many derives from acetophenone, salicylaldehyde or other related compounds. Schiff's bases have special importance in the field of coordination chemistry as they form stable complexes with most transition metal ions and may have abilities to coordinate more than one metal ion by the azomethine group. What improves these interactions is the presence of an additional hydroxyl group close to the azomethine group. Both this increases the coordination ability through a chelate effect and can play as a bridge in between two metal ions. A survey of the literature shows that their complexes generally exhibit interesting electroluminescent, magnetic,

---

* Corresponding author at: Department of Material Sciences, Faculty of Science and Technology, Abbes Laghrour-Khenchela University, Khenchela 40000, Algeria.
E-mail address: rym_46@hotmail.com (R. Benali-Cherif).

https://doi.org/10.1016/j.inoche.2022.110198
Received 12 August 2022; Received in revised form 9 October 2022; Accepted 5 November 2022

Table 1
Main crystallographic data and structure refinement details for $[Mn^{II}(L)_2(NO_3)(H_2O)_3]NO_3$.

Crystal data	$[Mn^{II}(L)_2(NO_3)(H_2O)_3]$ NO_3
Chemical Formula	$C_{26}H_{28}MnN_7O_8 \cdot NO_3$
Molecular weight (g/mol)	683.50
Diffractometer,	Xcalibur, Onyx
Radiation type	Mo Kα ($\lambda = 0.71073$ Å)
T (K)	293(2)
Calculated density (Mg/m^3)	1.332
Crystal system	Monoclinic
Space group	P 21/n
a (Å)	15.0256 (11)
b (Å)	11.7747 (8)
c (Å)	17.3421 (14)
β (°)	103.900 (8)
V (Å^3)	2978.3 (4)
Z	4
μ (mm^{-1})	0.50
Crystal size (mm)	0.15 × 0.10 × 0.08
No. of measured, independent and observed [$I > 2\sigma(I)$] reflections	17277, 7055 5308
R(int)[a]	0.037
Refinement	
$R[F^2 > 2\sigma(F^2)]$[b], $wR(F^2)$[c], S[d]	0.046, 0.156, 1.00
No. of unique reflections	7055
No. of parameters	422
$\Delta\rho_{max}$, $\Delta\rho_{min}$ (e Å^{-3})	0.61, −0.39

[a] $R(int) = \Sigma(Fo^2 - \langle Fo^2 \rangle)]/\Sigma(Fo^2)$.

[b] $R_1 = \Sigma||Fo| - |Fc||/\Sigma|Fo|$.

[c] $wR_2 = \{[\Sigma w(Fo^2 - Fc^2)^2]/[\Sigma w(Fo^2)^2]\}^{1/2}$.

[d] Goodness-of-fit $S = [\Sigma w(Fo^2 - Fc^2)^2/(n - p)]^{1/2}$, where n is the number of reflections and p the number of parameters.

catalytic properties [1], and important biological and pharmacological application [2–5]. Further, versatile applications of Schiff bases and their metal complexes in the treatment of diseases opened a new era in medicinal science [6]. Moreover, Schiff base compounds have been shown to be interesting molecules for the conception of more efficient, antibacterial, antianthrax, antifungal, antiviral, anticonvulsant, anticancer, antiprotozoal, antimycobacterial, anthelmintic, analgesic and antiplatelet treatments [7]. Schiff's bases are also important compounds due to their wide range of industrial applications [8] such as the photostabilization of polymers poly (vinyl chloride) against ultraviolet photodegradation [9,10]. Meanwhile, since 1952, isoniazid (**1**) has been an effective drug used against mycobacterium tuberculosis (MTB). It is used with a combination of medicaments to treat tuberculosis (TB). Mycobacterium tuberculosis (MTB) contains long chain -alkyl-hydroxy and fatty acids of 60–90 carbon atoms, these are mycolic acids [11]. Previous studies by others have shown that Schiff's bases of isoniazid and some of their metal complexes derivatives have antitubercular, antibacterial, antifungal and cytotoxic activities [12,13] as well as urease inhibitory activity and analgesic properties [14].

With the motivation to complement these results, we synthesized the Schiff's base resulting from condensation of isoniazid with benzaldehyde (**2**) with aim to investigate the biological activity of its metal complexes. As part of this work, we report hereafter on a manganese (II) complex where this Schiff's base does not make any coordination involving the azomethine as reported elsewhere. Instead, it coordinates solely with the nitrogen atom of pyridine only of isoniazid moiety. This new complex was characterized by single-crystal X-ray diffraction studies, and a detailed structural study is presented. The cyclic graph-set descriptors of the intermolecular hydrogen bonding stabilizing **(3)** are also discussed. This is complemented by the *Hirshfeld* surface analysis to better understand the contribution of different intermolecular interactions. In addition, a theoretical study using density functional theory (DFT/PBEPBE) and LANL2DZ basis sets was performed and was compared to the experimental results. Furthermore, the electrochemical behaviour of **(3)** was studied by the technique of cyclic voltammetry. According to this method we show that **(3)** has indicated electroactive properties. Finally, molecular docking analysis was also used to control the action mode of (2) and (3), to support the binding and active site of the protein with these compounds.

2. Experimental

2.1. Materials and methods

All organic chemicals and solvents were used as received and without any purification, then ^{1}H NMR and ^{13}C NMR spectra were recorded in deuteron MD_3OD and DMSO on a Fourier ARX 400 spectrometer at 400 MHz for proton and 100 MHz for Carbon 13. FT-IR spectra were performed on by a JASCO FT/IR-4100 Fourier transform instrument from transparent tablets by pressing samples and adding KBr pellets in the region of 4000–400 cm^{-1}. UV–Visible spectrum of the complex and ligand in DMF and methanol was recorded in the region of 200–800 nm using a Hitachi U-2800 spectrophotometer. Chromatography (TLC) was executed on Merck silica gel 60 F_{254}. Melting points were calculated on an electro thermal capillary fine control apparatus. Cyclic voltammetry experiments were used a CHI 660E electrochemical workstation.

2.2. Synthesis

2.2.1. Preparation of ligand

Schiff's base (**2**) was synthesized by reflux heating in a polar solvent as follows according to reported method [15]. To the stirred solution of benzaldehyde (0.001 mol) in absolute ethanol (6 ml) was added a solution of isonicotinic hydrazine acid (0.002 mol) in absolute ethanol (6 ml) and the resulting colorless solution refluxed for 3 h. The product separated on evaporation of the solvent was filtered, washed with a small amount of cold methanol and dried under vacuum. Yield: 94 %. M. p. 193 °C. Elemental analysis data for $C_{13}H_{11}N_3O$ (FW = 225.09): calculated C, 69.32 %; H, 4.92 %; N, 18.66 %, O, 7.10 %. FT-IR (KBr, cm^{-1}): 3199, 3026, 1689, 1598, 1552, 1355, 1411, 763, 686. UV–vis: λ^{max} (nm) (A)(CH_3OH): 302.78 (3.21), 261.16 (0.12), 239.25 (0.13). ^{1}H NMR (DMSO, δ (ppm)): 12.06 (s, 1H, N—H), 8.90 (s, 2H, H_2-H_6), 8.83 (s, 1H, H-4′), 8.78 (s, 1H, HC=), 7.77 (s, 2H, $H_{3'}$-$H_{5'}$), 7.76 (s, 2H, H_3-H_5), 7.68 (s, 2H, $H_{2'}$-$H_{6'}$),^{13}C NMR (DMSO, δ (ppm)): 162.06 (C=O); 150.74 (C-2, C-6); 142.92 (C=N); 140.90 (C-4); 134.45 (C-1′); 130.41 (C-4′); 129.26 (C-3, C-5); 127.96 (C-3′, C-5′); 121.94 (C-2′, C-6′).

2.2.2. Preparation of coordination compound

Coordination compound $[Mn^{II}(L)_2(NO_3)(H_2O)_3]NO_3$ **(3)** was prepared by reacting the Schiff's base N^2-benzylidenyl isonicotinic acid hydrazide **(2)** with the metal ions (II) as follows. To a warm solution of ligand (0.23 g, 1 mmol) in ethanol (20 ml) was added a solution of ($Mn(NO_3)_2 \cdot 4H_2O$) (0.22 g, 1 mmol) in ethanol (20 ml). The mixture was stirred and heated under reflux, for 3 h on an oil bath at 80 °C. Along this, a precipitate formed which was filtered, washed with 20 ml of hot ethanol and dried in vacuo. The reaction process was followed by TLC technique with mixed solvents (acetic acid/petroleum ether). Yellow crystals, suitable for X-ray data collection, were grown after two weeks of slow evaporation of an ethanol solution of the compound **(3)**. Yield: 39 %. M.p. 254 °C. Molar conductance (Λ) 0.407 Ohm^{-1} cm^2 mol^{-1}. FT-IR (KBr, cm^{-1}): 3436, 3198, 3026, 1692, 1566/1492/1448, 766, 514, 474, 426. UV–vis: λ^{max} (nm) (A)(CH_3OH): 236.32, 294.25.

2.3. Single crystal X-ray diffraction and structure refinement details and analysis

The single crystal diffraction measurements were performed on a 4-circles XCalibur, Onyx diffractometer for **(3)** equipped with an Onyx detector with a graphite monochromatized MoKα radiation, $\lambda =$

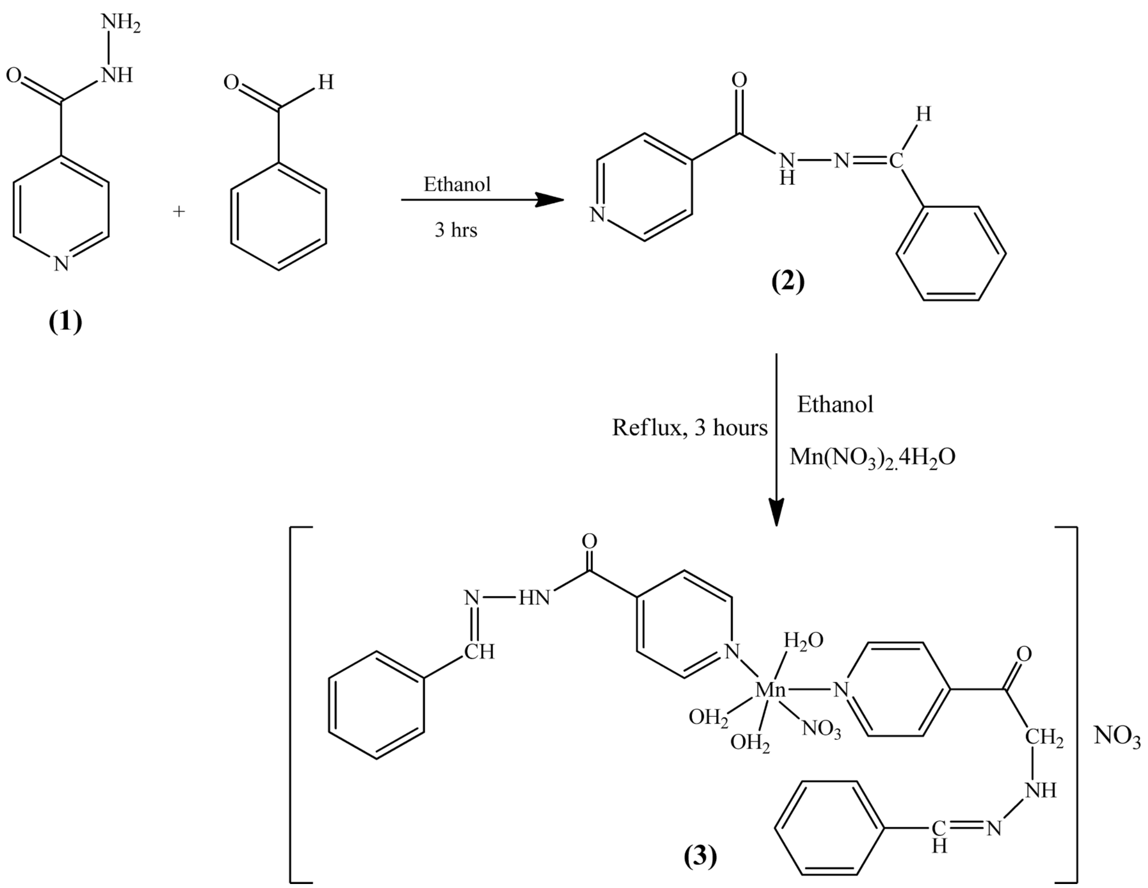

Fig. 1. General scheme of synthesis of **(3)**.

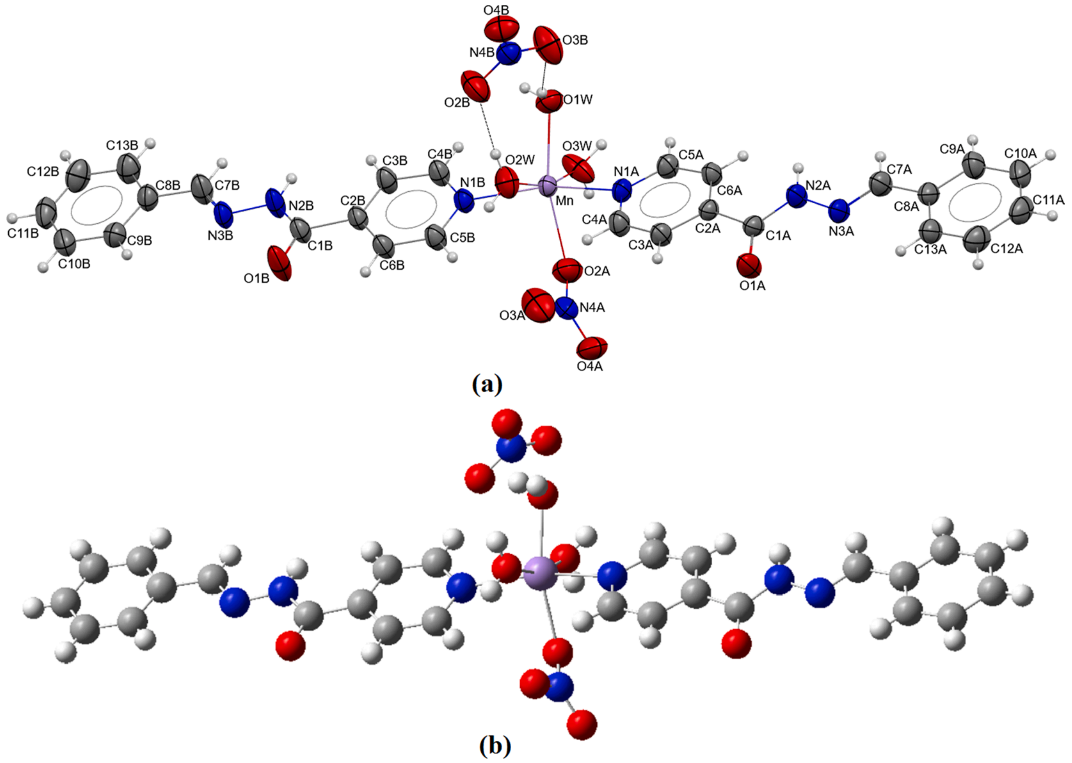

Fig. 2. (a) View of the asymmetric unit of **(3)**, showing the immediate intramolecular hydrogen-bonds. Displacement ellipsoids are drawn at the 50% probability level. (b) Optimized structure of **(3)**.

Table 2
Selected structural parameters, bond lengths (Å) and bond angles (°) in **(2)**.

Bond lengths DFT	Bond angles DFT
Mn—O3W 2.1330 (17) 2.0510	O3W—Mn—O1W 82.32 (7) 88.19
Mn—O1W 2.1549 (16) 2.0237	O3W—Mn—O2W 164.09 (8) 173.96
Mn—O2W 2.1736 (16) 2.1732	O1W—Mn—O2W 83.59 (7) 97.64
Mn—O2A 2.2577 (19) 2.0585	O3W—Mn—O2A 84.66 (8) 76.05
Mn—N1B 2.2821 (17) 1.9613	O1W—Mn—O2A 163.56 (7) 174.53
Mn—N1A 2.3097 (17) 1.9969	O2W—Mn—O2A 110.45 (7) 99.11
N4B—O3B 1.217 (2) 1.293	O3W—Mn—N1B 93.18 (7) 89.40
N4B—O4B 1.238 (2) 1.342	O1W—Mn—N1B 102.33 (6) 88.96
N4B—O2B 1.239 (2) 1.322	O2W—Mn—N1B 82.65 (7) 89.15
N4A—O2A 1.234 (3) 1.393	O2A—Mn—N1B 88.33 (7) 92.46
N4A—O3A 1.246 (3) 1.327	O3W—Mn—N1A 104.22 (7) 92.32
N4A—O4A 1.228 (3) 1.277	O1W—Mn—N1A 88.68 (6) 87.70
	O2W—Mn—N1A 82.75 (7) 89.55
	O2A—Mn—N1A 84.83 (7) 90.68
	N1B—Mn—N1A 160.58 (7) 176.24

Table 3
Selected hydrogen bonds parameters (Å, °).

D—H···*A*	*D*—H (Å)	H···*A* (Å)	*D*···*A* (Å)	*D*—H···*A*(°)
O1W—H1WA···O1B^{i}	0.85	1.89	2.694 (2)	158
O2W—H2WA···O2B	0.85	1.92	2.772 (3)	175
O3W—H3WA···O1A^{ii}	0.85	1.88	2.714 (2)	165
O1W—H1WB···O3B	0.85	2.08	2.853 (3)	151
O2W—H2WB···O2B	0.85	2.27	2.865 (3)	126.3
O3W—H3WB···O4A^{ii}	0.85	2.22	2.874 (2)	133.5
N2B—H2B···O4B^{iii}	0.86	2.17	2.976 (3)	156
O2W—H2WB···O4B^{iii}	0.85	2.173	3.020 (3)	173.9
N2A—H2A···O4A^{ii}	0.86	2.28	3.048 (3)	148
C7B—H7B···O4B^{iii}	0.93	2.46	3.275 (3)	146
C5B—H5B···O4B^{iv}	0.93	2.58	3.284 (3)	133
C7A—H7A···O3A^{ii}	0.93	2.48	3.385 (3)	163
C5A—H5A···O1A^{ii}	0.93	2.57	3.470(3)	161.5

Symmetry codes: **(i)** $-x + {}^{3}/_{2}$, $y - {}^{1}/_{2}$, $-z + {}^{3}/_{2}$; **(ii)** $-x + {}^{3}/_{2}$, $y - {}^{1}/_{2}$, $-z + {}^{1}/_{2}$; **(iii)** $x + {}^{1}/_{2}$, $-y + {}^{1}/_{2}$, $z + {}^{1}/_{2}$, **(iv)** $-x + 1$, $-y + 1$, $-z + 1$.

0.71073 Å. Crystal data, data collection and structure refinement details of **(3)** are summarized in Table 1. The structure has been solved in the space groups $P2_1/n$ by dual-space method using the program SHELXT [16], and successive Fourier difference syntheses, and were refined against F^2 by weighted full-matrix least squares methods including all reflections with SHELXL-2018 program [17]. All calculations were carried out using Olex2 1.3 software package [18]. Structural representations were drawn using Mercury [19]. All absorption corrections were performed with the multi-scan program [20]. All non-H atoms were refined anisotropically. All hydrogen atoms were located in difference density Fourier maps. Analysis of intermolecular interactions using the Hirshfeld surface (HS) was carried with Crystal Explorer software to compute external, d_e, and internal, d_i, distances of atoms to the surface [21].

2.4. *Theoretical calculations*

All quantum chemical studies were performed with the Gaussian package 09 [22]. Gauss View 5.08 has been used for the visualization of the structure and the simulation of vibratory spectra. The optimized geometry and electronic structure of complex (**3**) in the gas phase were carried out using the Density Functional Theory (DFT/PBE0) with LANL2DZ pseudo-potential and the associated basis set which was used for metal atoms [23,24]. Additionally, Schiff's base linked to the metal was optimized using the same level of theory. The vibrational modes of (**3**) were determined by using the total energy distribution (TED) [25,26]. Furthermore, quantum chemical descriptors that include energy gap (ΔE_{gap}), hardness (η), softness (S), global electronegativity (χ), and electrophilicity (ω) have also been computed by the same approach that in the works of literature [27].

2.5. *Cyclic voltammetry*

Cyclic voltammetry (CV) of title compound were conducted in DMSO with 0.10 M potassium chloride as the supporting electrolyte. Electrochemical experiments were conducted in a three-component cell consisting of a Pt wire auxiliary electrode, a glassy carbon (GC) as working electrode in the range of − 0.1 to +0.1 V [28]. The ligand and complex were investigated at room temperature. The voltammograms were recorded at a potential scan rate of 100 mV·s^{-1}.

2.6. *Molecular docking*

Molecular docking is a very important method that can be used to

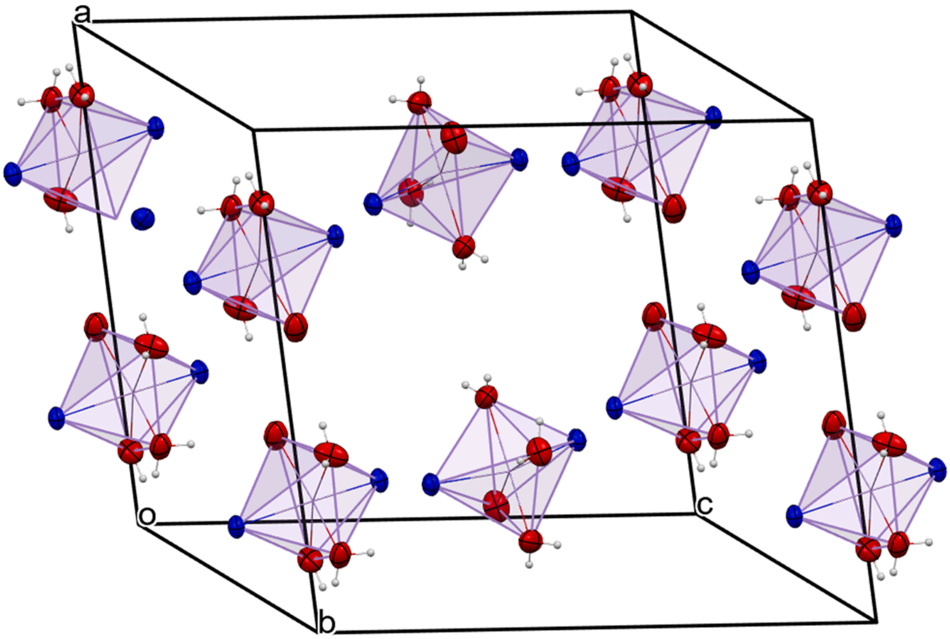

Fig. 3. MnO_4N_2 Octahedrons positioning in the lattice structure.

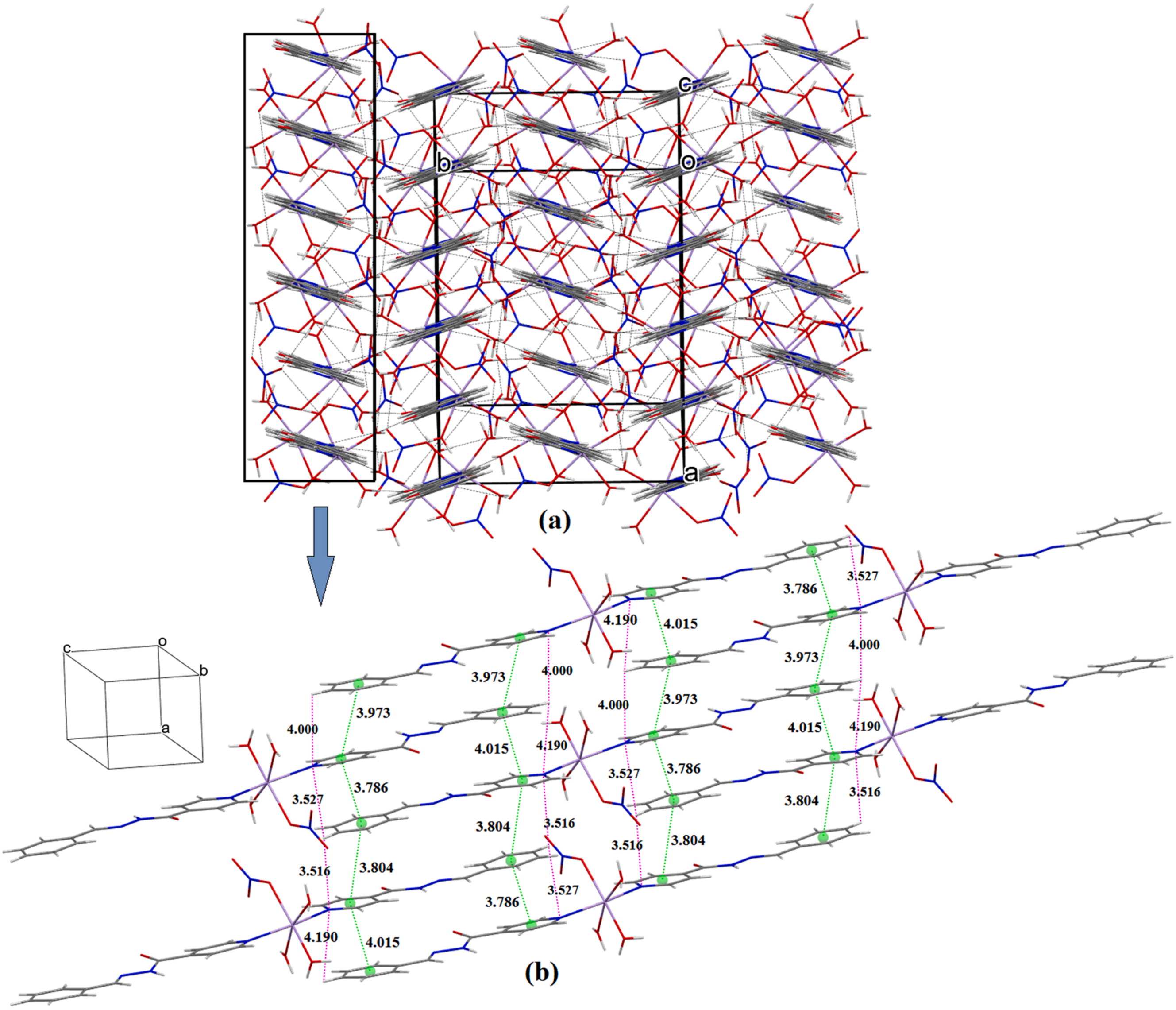

Fig. 4. (a) A view of the crystal packing of **(3)** showing the dense hydrogen bonds network and the organic cations stacking. (b) Supramolecular layered assembly of **(3)** showing the role of aromatic π—π stacking and $N_{lone\text{-}pair}\cdots C—H$ intermolecular electrostatic interactions in stabilizing the crystal packing. The distances are measured in Å.

predict the binding affinity between a selected biological target and active ingredients. The compounds **(2)** and **(3)** were targeted to the 2X22 enzyme involved in Mycobacterium tuberculosis H37Rv. InhA, the enoyl-ACP reductase from mycobacterium tuberculosis which is the isoniazid drug target for the treatment of this disease [29]. Docking studies of all synthesized compounds were carried out using Molegro Virtual Docker MVD 2019.7.0 software. The structure of the protein database (PDB code: 2X22), and the three-dimensional structure of **(2)** and **(3)** was performed by ChemDraw 3D. PyMOL 1.9.0.0 software to remove all bound water.

3. Results and discussion

3.1. *Structure and crystal packing*

The asymmetric unit of **(3)** consists of a nitrate anion and a complex cation $[Mn^{II}(L)_2(NO_3)\,(H_2O)_3]^+$ as illustrated with atomic numbering in Fig. 2. Crystallographic data, measurements and refinement details of the coordination compound are presented in Table 1. Selected bond distances and angles for **(3)** are given in Table 2 whereas hydrogen bonding interactions that stabilize the crystal structure are listed in Table 3. X-ray crystal structure analysis reveals that the complex crystallizes in the monoclinic space group $P2_1/n$.

The complex reveals a six coordinate manganese (II) centre. Two isonicotinic acid benzylidene-hydrazide ligands are coordinated via two pyridine nitrogen atoms (N1A, N1B) to the Mn(II) while the remaining coordination sites are occupied by four oxygen atoms from three water molecules and one nitrate anion in such a way the complex lack symmetry centre. The asymmetric unit cohesion is ensured by two strong O—H···O hydrogen bonds established between the nitrate anion and two coordinated aqua ligands (Fig. 2).

The coordination geometry around the Mn (II) ion can be described as a distorted octahedral environment. The manganese is surrounded in octahedral arrangement by two $N_{pyridine}$ atoms, one O atom of the nitrate anion and three water molecules. The geometrical features of the MnO_4N_2 octahedron are reported in Table 2. The N—Mn—O and O—Mn—O angles range respectively from 82.63(7)° to 104.24(7)° and 82.34(7)° to 110.47(7)°.

The bond distances between manganese and water molecule varies from 2.133(2) Å to 2.173(2) Å, these distances Mn (II)—O_{Water} are lower

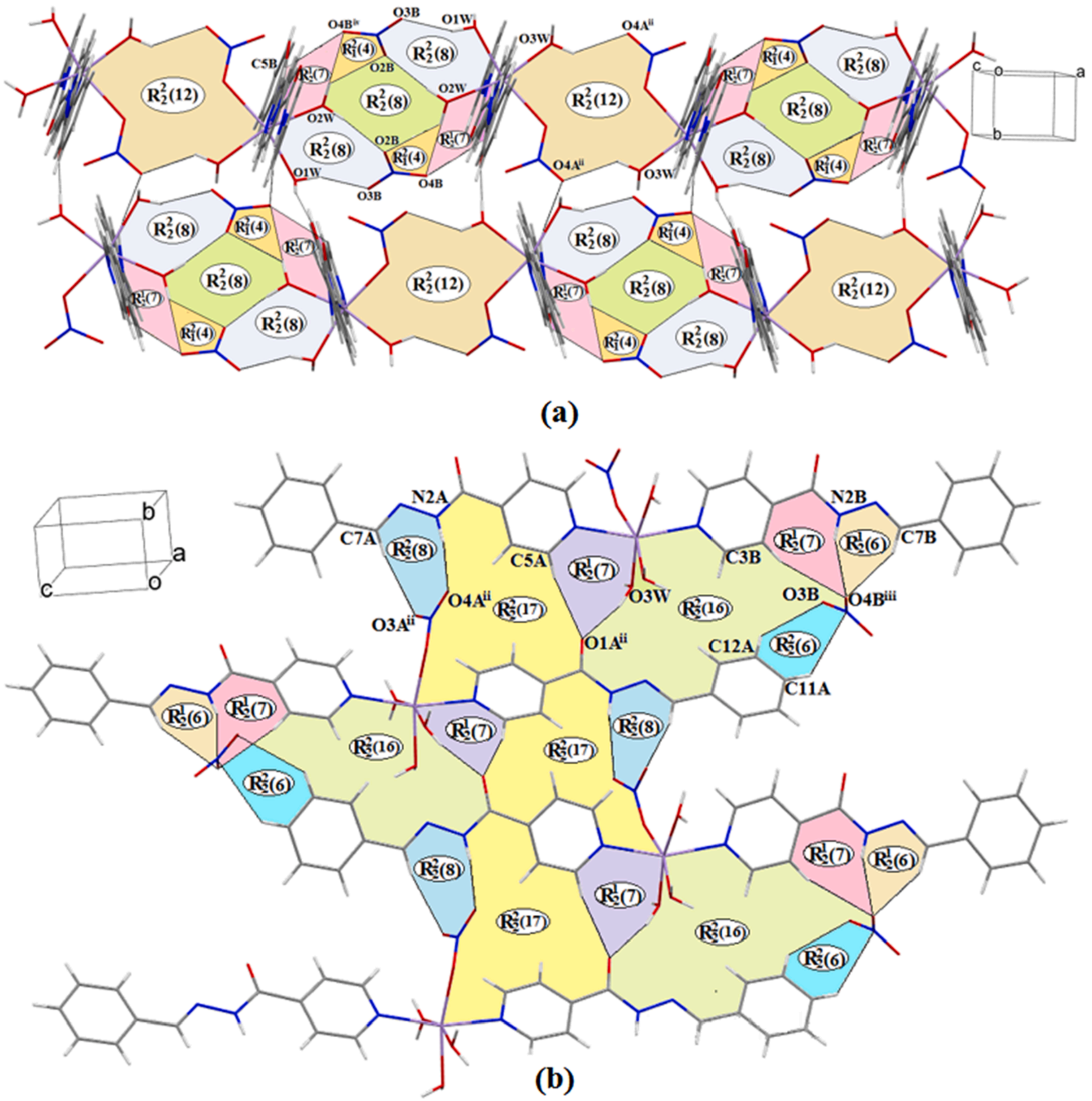

Fig. 5. Parts of packing diagram of **(3)** showing the supramolecular synthons and the graph set describing intermolecular interactions. (a) Apical plane (b) Equatorial plane.

than that observed between Mn (II)—$O_{\text{Nitrate anion}}$ with a value of 2.258 (2) Å. Whereas the two bond distances between manganese and pyridine nitrogen are 2.311(2) Å and 2.284 (2) Å. These values clearly indicate the distorted octahedral geometry of MnO_4N_2 species. The detailed geometry of the MnO_4N_2 octahedra (Table 2) shows that the bond distances compare to those reported for similar octahedral Mn (II) complexes [30]. It is worth to note that in the lattice structure, the MnO_4N_2 entities are situated on the unit cell edges in $^1/_3$ **a** and $^2/_3$ **a** positions, and inside the unit cell at (¼, ½, ½) and (¾, ½, ½) (Fig. 3).

The great abundance of hydrogen bonding donors and acceptors origins a complex three-dimensional hydrogen bonding network (Fig. 4a). The molecules interact with one another by means of hydrogen bonding and electrostatic interactions. The crystal packing of organic cation displays an alternating of two cationic layers parallel to the planes formed by **c** + ¼ **a** and ¼ **a** + ½ **b** + **c** directions (Fig. 4a). The planes of the organic cation show two orientations, related by a 2-fold helicoidal axis along **b**.

Complex cations $[Mn^{II}(L)_2(NO_3)(H_2O)_3]^+$ are stacked together through an inversion center to form a supramolecular stacked ribbon parallel to the [1 0 4] and [1 2 4] directions. The molecules involved in individual parallel one-dimensional chains are in contact with the partner molecule belonging to the neighbouring chains by π-stacking interactions. It is found that the π···π stacking interaction as the centroid-to-centroid separation ranges from 3.786 (3) Å to 4.015 **(3)** Å (Fig. 4b). The interconnection of the monomeric units *benzene rings···benzene rings* and *pyridine···pyridine* through these weak interactions between the molecules defining connected columns along the ***a*** crystallographic axis (Fig. 4a and b). Moreover, the nitrogen atoms from the pyridine ring exhibit electrostatic contacts with benzene rings through $N_{\text{lone-pair}}\cdots$H—C interactions with distances ranging from 3.516 (2) Å to 4.190 (2) Å (Fig. 4b).

In the apical plane of **(3)** the cations are arranged into; a centrosymmetric homosynthon $R^2_2(12)$ ring motifs [31] through a double O3W—H3WB···O4A^{ii} ($d_{D\cdots A}$ = 2.853(2) and 2.874(2) Å and symmetry code: **(ii)** −x + $^3/_2$, y − ½, −z + ½) interactions established between the related nitrate group and the coordinated water molecule (Fig. 5a). On

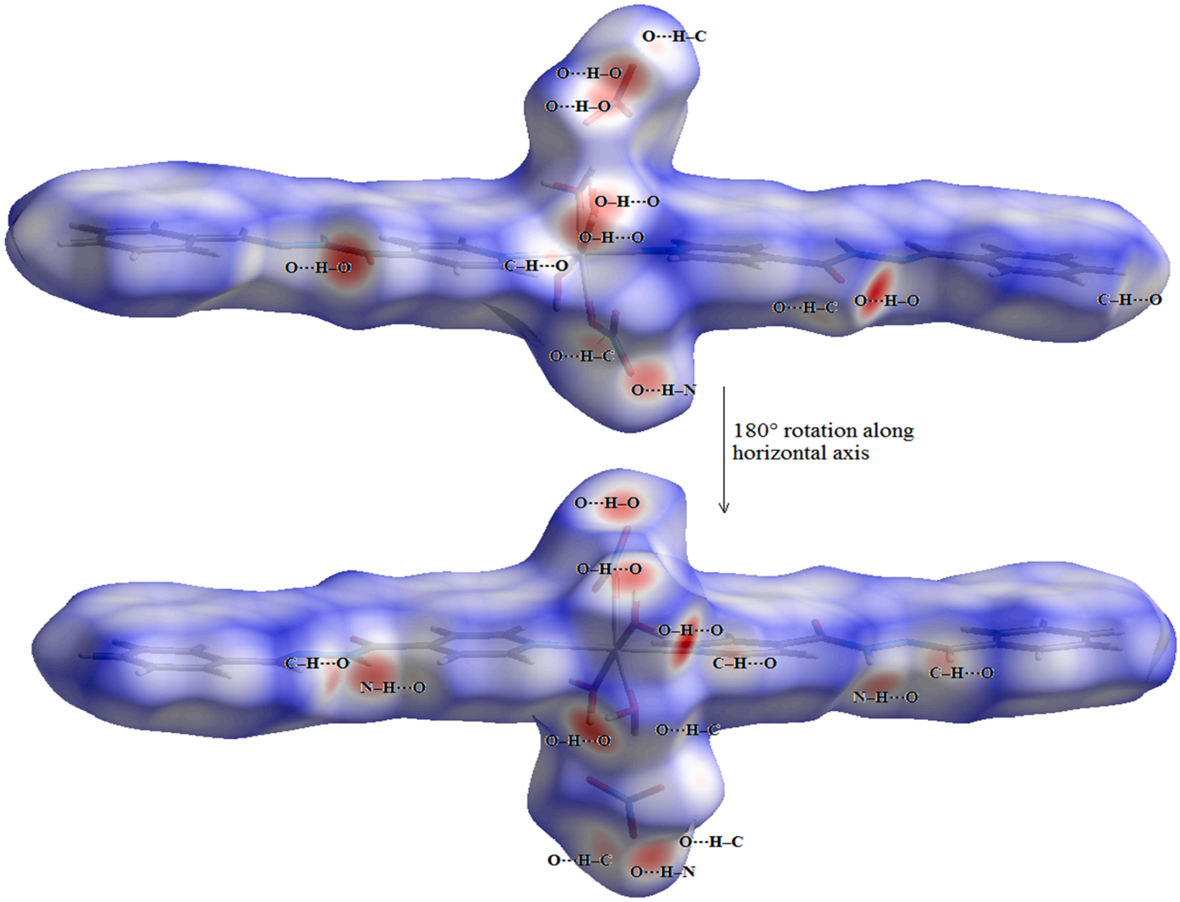

Fig. 6. Two different views of HS mapped with d_{norm} of compound (**3**) showing the intermolecular interactions (D–H···A when the donor is inside the surface, and A···H–D when the donor is outside it).

the other hand, the $[Mn^{II}(L)_2(H_2O)_3(NO_3)]^+$ cation interacts with the nitrate ion via its two remaining coordinated aqua ligands through O1W—H1WB···O3B ($d_{D\cdots A}$ = 2.853(3) Å) and O2W—H2WA···O2B ($d_{D\cdots A}$ = 2.772 (3) Å) hydrogen bonds giving rise to an $R_2^2(8)$ heterosynthon motif. Furthermore, the previous cation is a three times hydrogen bonds donor with a second uncoordinated nitrate ion linked to the first by an inversion center via the pairs O2W—H2WB···O2B/O2W—H2WB···O4B^{iii} and O2W—H2WB···O4B^{iii}/C5B—H5B···O4B^{iv} thereby generating respectively an $R_1^2(4)$ and $R_2^1(7)$ heterosynthon motifs that contains both strong and weak interactions. In addition, another $R_2^2(8)$ ring type is created by the combination of the last three graphs as well their inversion-related motifs (Fig. 5a).

In the equatorial plane, the manganese complexes ribbons are packed in the crystal and connected to each other by intramolecular interactions involving the acceptors O3A and O4A atoms from the coordinated nitrate group and O1A atom from the related isonicotinic acid benzylidene-hydrazide ligands where their combination generate $R_2^2(8)$, $R_2^2(17)$ and $R_2^1(7)$, graph set. A large view of the packing clearly shows that these rings illustrate how the neighboring ribbons link to each other through the N2A—H2A···O4A^{ii}, C7A—H7A···O3A^{ii}, C5A—H5A···O1A^{ii} and O3W—H3WA···O1A^{ii} intermolecular interactions (Fig. 5b).

Additionally, the nitrate anions also contribute to the ribbons cohesion by means of strong, weak and non-conventional interactions, on the one hand by forming three cyclic hetero-synthon $R_2^1(7)$, $R_2^1(6)$ hydrogen-bonding motifs and on the other hand by building one supramolecular hetero-synthon $R_2^2(6)$ ring motifs. Another ring is formed by means of the intermediate cation-cation and cation–anion-cation interactions where their combination generates an $R_2^2(16)$ graph-set motifs (Fig. 5b). Therefore, each manganese complexes are bonded to another through intermolecular hydrogen bondings, among these interactions are those that involve coordinated water ligands and uncoordinated nitrates as shown in Fig. 5. This kind of interactions are found to stabilize the structures [32].

In crystal lattice of **(3)**, nitrates anions play an important role in complementing the noncovalent binding forces in stabilization. The propagation of the low-dimensional structure to a 2-D framework is basically due to strong hydrogen bonding interactions involving a variety of supramolecular synthons (Fig. 5a and b).

3.2. Hirshfeld surface analysis

Analysis of intermolecular interactions using the Hirshfeld surface (HS) is an effective way to quantify them and a principle tool to gain insights into understanding the three-dimensional crystal packing.

The HS of compound $[Mn^{II}(L)_2(NO_3)(H_2O)_3]NO_3$ have been exemplified in (Figs. 6 and 7), by showing d_{norm}, shape-index and curvedness surfaces. The intermolecular distance information on the surface can be condensed into a two-dimensional scatter diagram of external (d_e) and internal (d_i) distances of atoms to the surface [21] (Fig. 8).

The effective spots existing in the d_{norm} surfaces represent the hydrogen bonding interactions within the structures which are included in Table 3. The dark-red regions which are visible on the d_{norm} surfaces indicate the presence of O—H···O and N—H···O hydrogen bonds. whereas the small extent of area and the comparatively light-red spot on HS indicates the C—H···O interaction.

Not only hydrogen bonding interactions can be explored by HS analysis but also comparatively weak interactions involving phenyl rings can be explored. The presence of red and blue triangle pairs on the back and front views on the HS plotted over the shape index (Fig. 7A)

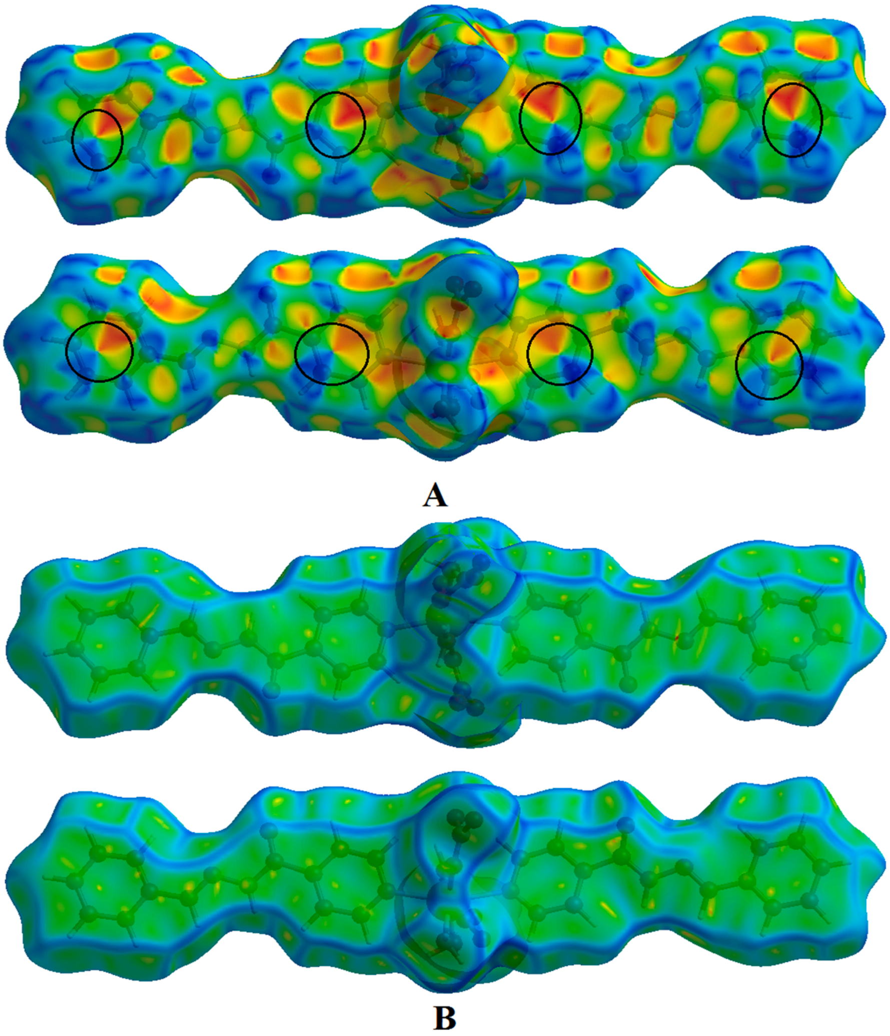

Fig. 7. HS highlighting the presence of π-π aromatic stacking between phenyl rings mapped with (A) shape index (the bicolor triangle pairs surrounded by the black circles) and (B) curvedness.

around phenyl rings indicate that π···π stacking interactions are present in the crystal packing,

Moreover, fingerprint plot (FP) [33] has been adopted by many researchers as a way of quantifying the relative importance of various interactions present in the molecular packing such as O···H, H···H, N···H, C···H, C···C. FP plots are extremely sensitive to the immediate environment of a molecule in a crystal, and they are unique for a given molecule in a particular crystal. Taking advantage of this uniqueness, FP have been found to be useful in studies involving comparisons between hybrid compounds [34,35].

Fig. 8 is picturizing the 2D FP plots of the title compound which highlight separately the most important intermolecular contacts. The FP present a symmetric behavior where the two distinct sharp peaks projecting towards the bottom of the fingerprint plot are due to strong O—H···O hydrogen bonds. This analysis shows that the O···H intercontact contribute in largest value to the Hirshfeld surface with 37.2 %. The presence of these long spikes characteristic of strong hydrogen bonds which exhibits the shortest contacts at *ca* 1.753 Å associated with the O3W—H3WA···O1A and O1W—H1WA···O1B interactions.

The other visible light-white regions in the d_{norm} surfaces are indicative of weaker as well as longer contacts other than hydrogen bonds viz. H···H interactions. They are the second most frequent interactions covering 30.5 % due to the abundance of hydrogen on the molecular surface. This abundance also explains the spike elongation on the d_e/d_i diagonal line.

The characteristic shape of H···C looks like symmetrical 'wings', include 11 % of total HS area and with the closest contacts at approximately 3.02 Å.

Further, the C···C inter-contacts appear as distinct triangle in the FP, and correspond to the π···π stacking interactions which constitute the fourth most occurrent contacts in the packing, this is justified by the presence of red and blue triangle pairs on the back and front views of the shape index representation (Fig. 7A). The presence of π···π stacking is also evident because of a flat region toward the bottom of both sides of the molecule and is clearly visible on the curvedness surfaces (Fig. 7B).

The N…H and H…N contacts combined appear as a symmetric spike, on the top left and bottom right of the related plots, and their proportion of about 6.3 % resulting from the C—H…$\mathrm{N}_{\text{lone-pair}}$/$\mathrm{N}_{\text{lone-pair}}$…H—C intermolecular electrostatic interactions which correspond to a short length of 2.503 Å. Further, the presence of the N…N contacts reflects the presence of *van der Waals* lone-pair …lone-pair interactions, which comprise 1.5 % of the total HS area with $d_e + d_i \sim 3.678$ Å. In addition, the contacts of C…N/N…C, C…O/O…C, N…O/O…N and O…O are of low meaning as they are derived from less important interactions with small contributions in the all parts of HS.

3.3. Spectroscopic analyses

The manganese complex was easily synthesized by the reaction of Schiff's bases and metal nitrate by heating under reflux. This complex is

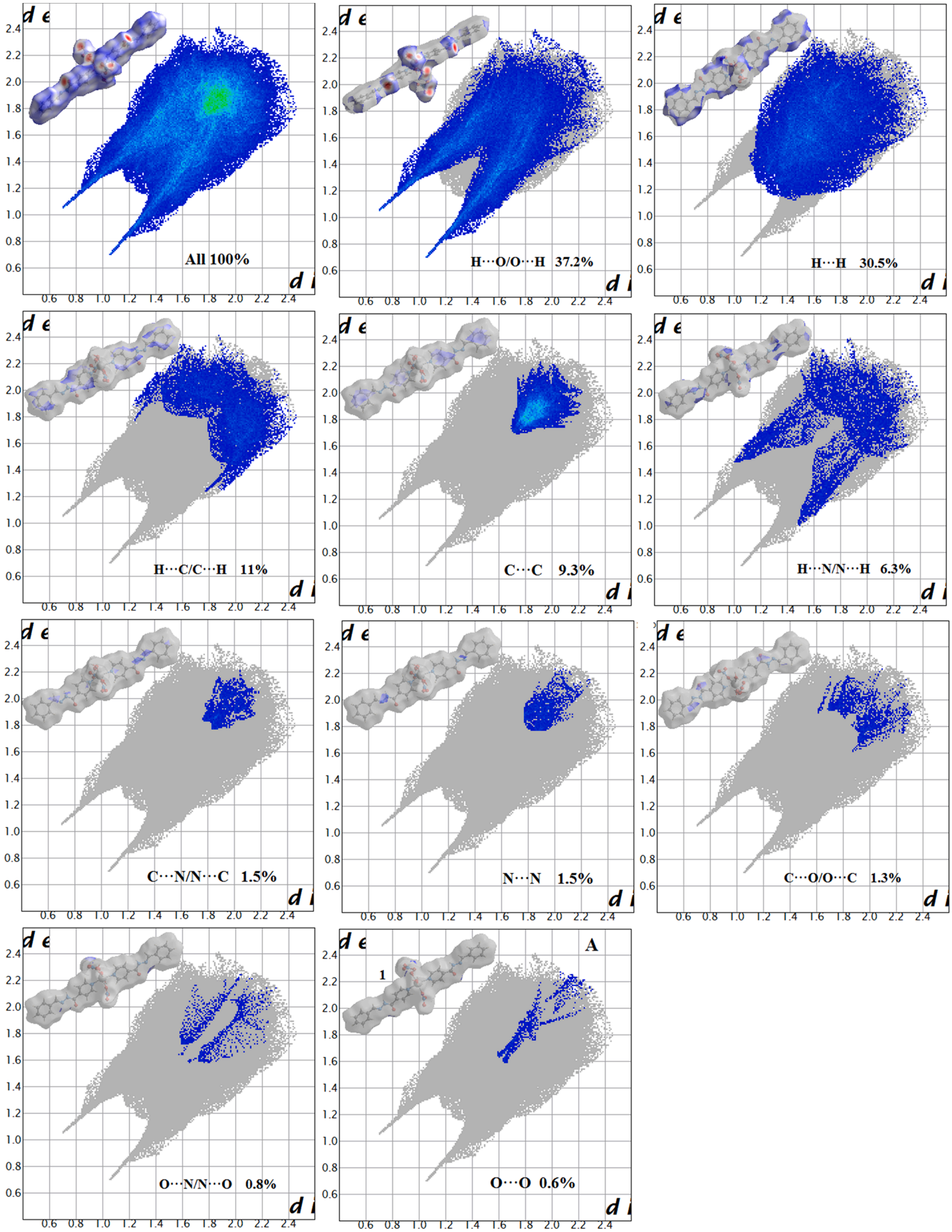

Fig. 8. 2D fingerprint plots of the HS around the asymmetric unit; the areas of all the intermolecular contact present are clearly shown, the surfaces to the top left highlight the relevant surface patches associated.

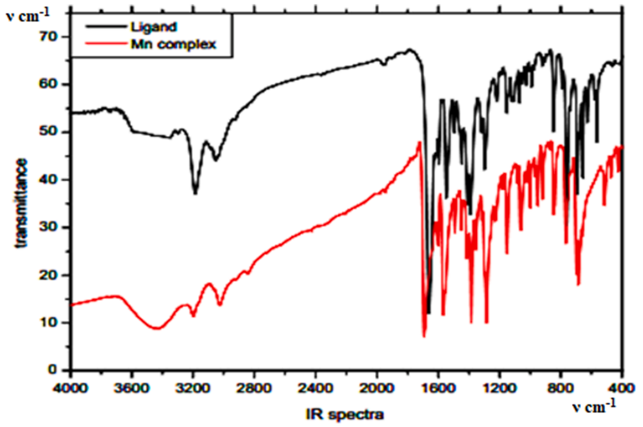

Fig. 9. FT-IR Spectrum of ligand [(**2**) black line] and their complex [(**3**) red line)]. (For interpretation of the references to colour in this figure legend, the reader is referred to the web version of this article.)

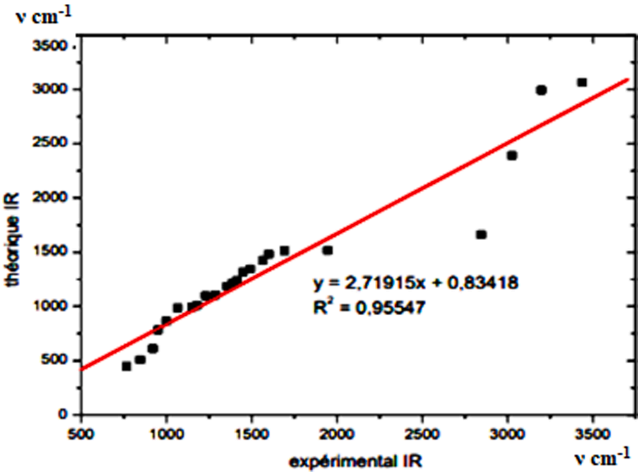

Fig.10. The linear regression between the calculated (scaled) and experimental frequencies of title compound (**3**).

very stable at room temperature in the solid state and is insoluble in common organic solvents, methanol, ethanol and chloroform, but there is very soluble in DMF and DMSO. In this research, the room temperature method was not used which did not give the crystalline form of the complex, on the other hand heating at reflux shows the efficiency of crystallization rapidly with a remarkable high yield. The metal complex (II) with this ligand is new and therefore reported for the first time.

3.3.1. *Infrared spectra*

The IR spectra of the type hydrazone ligand showed band characteristic of the expected functional groups and the vibrations data are given in spectrum (Fig. 9). In order to study the binding mode of the ligand compound (**2**) (Fig. 1) we showed characteristic broad band at 3186 cm^{-1} attributed to the N—H vibration, the stretching bands of νC—H, νC═O, νC═N displayed respectively at 3030 cm^{-1}, 1665 cm^{-1} and 1554 cm^{-1} [36,37]. Also, the appearance of C═N vibration in the FT-IR spectrum confirm that the ligand formed in the azomethine (imine). The IR spectrum of **(3)** show a characteristic band at 3436 cm^{-1} that can be attributed to ν(HO) indicating the presence of coordinated water molecules in the compound which was not present in the ligand [37]. The NH band in the complex occurs at 3198 cm^{-1} which shows that it does not make a coordination or hydrogen bonds. However, the stretching bands increased by small values of νC—H, νC═O, νC═N indicating these atoms do not take participate in the coordination. In addition, a strong sharp band of the IR spectra of Mn complex showed at 1384 cm^{-1} that can be attributed to an uncoordinated nitrate ion [38]. The band at 1656 cm^{-1} corresponding to monodentate nitrate [39]. The experimental modes are very good agreement with the scaled ones. The calculated modes are very good agreement with the experimental ones. The correlation graphic was plotted between the calculated and experimental wavenumbers obtained by DFT/PBEPBE method. The correlation between the scaled and experimental frequencies is plotted in (Fig. 10). From this graph, a remarkable linearity was found between the experimental and calculated frequencies. The correlation coefficient (R^2) is 0.95547. We can conclude that the calculated frequencies are consistent with the experimental ones Fig. 11.

3.3.2. *UV–Visible spectra*

The electron absorption spectra of ligand and its Mn (II) complex were recorded at room temperature using DMSO as solvent. The UV–Visible spectra of Schiff base ligand showed absorption bands at 336.46 nm is due to the π–π* transition in benzene and pyridine the second bands at 239.26 nm and 261.16 nm are assignable to n–π* transition nonbonding electrons presents on the nitrogen of the azomethine chromophore (—C═N) [40]. The Mn (II) complex showed absorption band at 294.25 nm, 236.32 nm of intra ligand and other band at 898.36 nm assigning to these absorptions is most complexation ligand-to-metal electronic transfer. These are conforming the octahedral geometry [41,42].

3.4. *Cyclic voltammetry*

The CV of the Schiff base ligand **(2)** (Fig. 12) which exhibited only

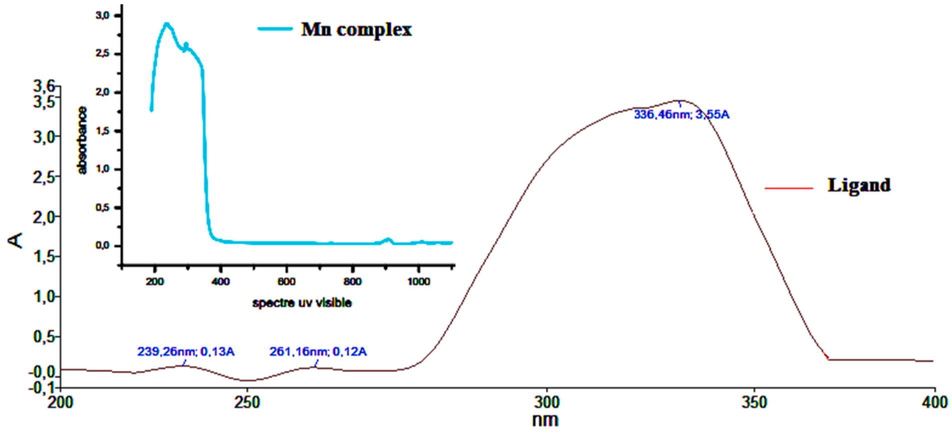

Fig. 11. The UV–visible spectra of ligand **(2)** and coordination compound **(3)**.

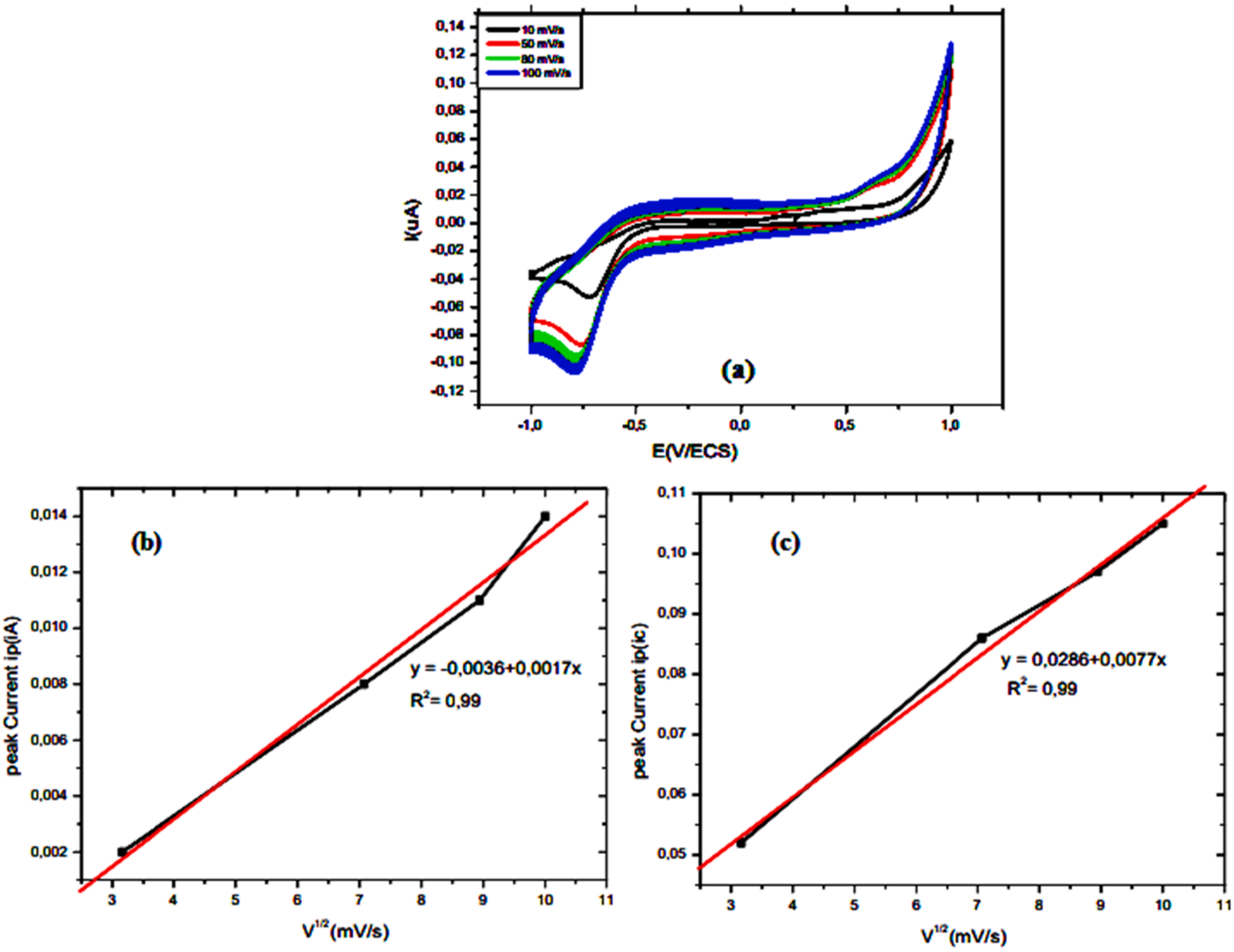

Fig. 12. Cyclic voltammograms recorded for 1.0 M ligand (**2**) at a classy carbon electrode DMSO containing 0.1 M KCl. (a) At scan rates 100 m/s, (b, c) plots of anodic (I_{pa}) and cathodic (I_{pc}) peak currents versus square root of the scan rate ($V^{1/2}$).

one irreversible reduction peaks at Epc = −700 mV to −790 mV at 10 mVs^{-1} to 100 mVs^{-1}. We can notice the absence of anode peak potential (Epa) corresponding to the cathode peak potential means that the system is totally irreversible, which can be explained as a two-electron reduction process of the azomethine group (C═N) into unsaturated system [43]. The current anodic peak evolves linearly as a function of the scanning speeds passing through the origin as well as the ratio of the anodic and cathodic currents Ipa/Ipc which vary to reach unity, thus suggesting the convergence of this redox system towards a reversibility.

A cyclic voltammogram of the Mn complex (Fig. 13) show two anodic waves at E_{pa1} = 220.1 mV and E_{pa2} = 817.3 mV. The first one can be assigned to the oxidation of Mn (II) to Mn (III) but the second was attributed to the oxidation of azomethine group [44]. On the cathodic side, two peaks were observed at E_{pc1} = -307.4 mV and E_{pc2} = 521.1 mV which correspond to the reduction of Mn (III) to Mn (II) and the reduction of the azomethine group, respectively [44]. The anodic and cathodic current were linearly increased with the square root of the scan rate from 10 to 100 mV s^{-1}, while for higher scan rates, so the electrochemical reaction is diffusion-controlled process [45]. The values of the electrochemical parameters characteristics of the voltammogram corresponding to the oxidation of the complex, recorded in the range of potentials ranging from −200 to −1300 mV are grouped together in Table 4 given below.

3.5. *DFT computational analysis*

The optimized geometry of the studied complex is shown in Fig. 14 with the central bond length in Ångström. Metal-ligand bond distances obtained agreement with experimental bond distances (Table 2). In this study we compared the experimental values obtained by X-ray diffraction with the theoretical values which are calculated by DFT/PBEPBE and LANL2DZ basis sets. In addition, this study can also explain the chemical concept of the highest occupied molecular orbital (HOMO) and the lowest unoccupied molecular orbital (LUMO) are keys values on the electron donor and acceptor character of complexes in general and which will lead to the interpretation of the charge transfer process. This makes it possible to define the chemical stability of the compounds, and the energy difference between HOMO and LUMO (E_{gap}) shows the high stability of the complexes with respect to chemical reactions, a low ΔE (E_{LUMO} − E_{HOMO}) gap is well sought after by chemists, who concerns chemical reactivity in applications such as biological studies such as (antibacterial, antioxidants, etc.) due to the ability to encounter charge transfer interactions. It can be explained that **(3)** has a higher tendency to donate electrons to an electron-accepting species at poor sites. As can be seen in Fig. 14, the electronic density of **(3)** is mainly distributed over the central atom and the molecules of water and nitrates, for HOMO and LUMO. The calculated values of the reactivity descriptor parameters such as the ionization potential (I), electron affinity (A), absolute electronegativity (χ), absolute hardness (η), and softness (S), for **(3)** were calculated at the same levels, and the results are summarized in Table 5.

3.5.1. *Molecular electrostatic potential (MEP) and Mulliken charges analysis*

The Molecular electrostatic potential (MEP) surface of **(3)** is depicted

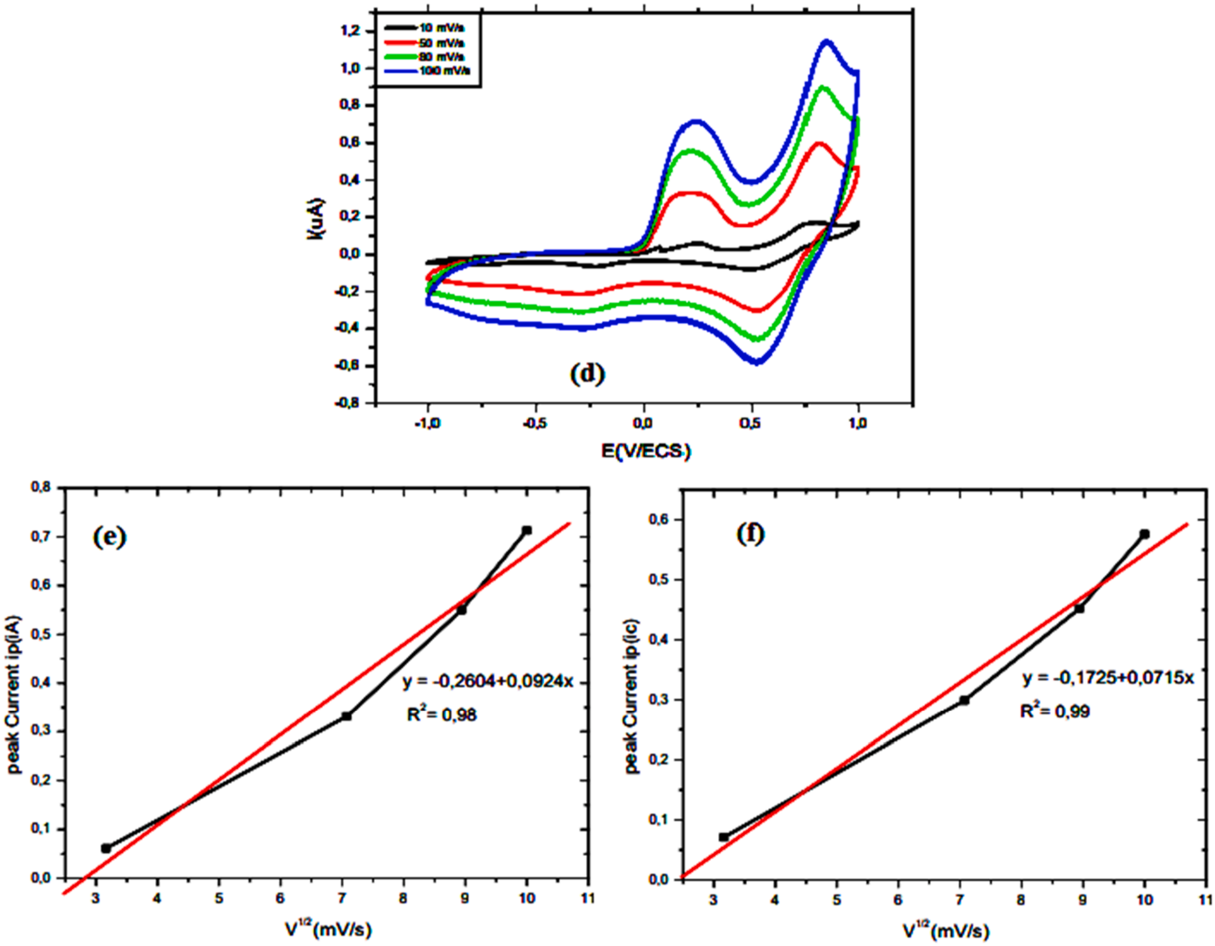

Fig. 13. Cyclic voltammograms recorded for 1.0 M of **(3)** at a classy carbon electrode DMSO containing 0.1 M KCl. (d) at scan rates 100 m/s, (e, f) plots of anodic (I_{pa}) and cathodic (I_{pc}) peak currents versus square root of the scan rate ($V^{1/2}$).

Table 4
Cyclic Votammetric data for **(3)**.

Scan Rate mV/s	E_{pa} mV	E_{pc} mV	ΔE_p mV	I_{pa} m/A	I_{pc} m/A	I_{pa}/I_{pc}
10	247.9	498.8	250.9	0.061	0.071	0.859
50	220.1	521.1	301	0.331	0.299	1.107
80	211.5	525.8	314.3	0.550	0.452	1.216
100	230.1	530.2	300.1	0.713	0.576	1.237

in Fig. 15. The MEP is widely used as a reactivity map displaying the most reactive sites for electrophilic attack on an organic molecule. The maps were obtained at the DFT/PBEPBE and LANL2DZ basis sets. As it can be seen, in each MEP surface is represented by different colors: red, blue and green represent the regions of negative, positive and zero electrostatic potential Figs. 16 and 17.

The most positive areas are on the protons of water molecules and the metal atom in particular; the negative areas are on the oxygen of nitrate and carbonyl function, in agreement with the Mulliken charges see below Table 6. The Mulliken charge distribution of all atoms in the asymmetric unit are listed and numbered as follows (Fig. 15b).

The atomic charge distribution shows that the manganese ion has a positive charge of 0.465, while the two nitrogen atoms of the pyridine cycle have negative charges of −0.194 and −0.223. The three oxygen atoms of the water molecules ligands have a negative charge of −0.684, −0.683 and −0.645 respectively, the 10O, 16O and 26O oxygen atoms of the nitrate group have negative charges of −0.165, −0.324 and −0.294. while the 8O atom of carbonyl group has a negative charge of −0.212. All hydrogen atoms carry positive charge in the range 0.229–0.450. These values are in agreement with the MEP results.

3.6. Molecular docking

Molecular docking *in silico* aims to predict the structure of a molecular complex from isolated molecules, which is considerably easier and faster than using one of the experimental methods. Docking software are therefore very useful tools in biology, pharmacy and medicine, because most of the active ingredients are small molecules (ligand) that interact with a biological target of therapeutic interest, usually protein (receptor), in order to influence the mechanism in which this protein is involved. In this study, we determine the possible action mode of the target compound ligand and its complex. Molecular docking of **(2)** and **(3)** were performed in the active site of Mycobacterium tuberculosis enoyl reductase InhA to examine their possible binding modes. The protein data bank file (PDB: 2X22) was selected for this intention. In order to gain more insights into the interactions, the synthesized compounds were docked into the active site of receptor. According to these results, the most effective intermolecular hydrogen bonds are observed between the ligand Schiff base through C═O atoms and lle B 21 and thy B 196, steric interactions bond with ala B 198, ser B 20, ser B 94 and lle B 16. Also, **(2)** demonstrated the most negative coupling score parameter against the 2X22 with value of −81.457 kcal/mol. It was found that both hydrogen bonding and steric interactions of Mn complex **(3)** with the largest molDock score −189.656 kcal/mol were considerably larger than ligand **(2)**. The Mn complex **(3)** made hydrogen bonds with gly B 192, lle B 194, try B 158 and ser B 94 amino acids. It has been observed

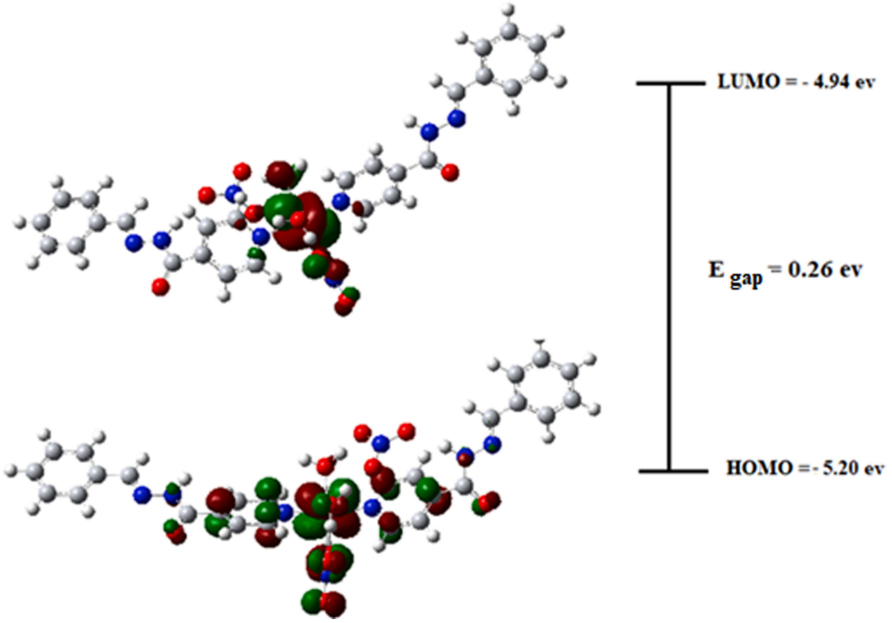

Fig. 14. HOMO-LUMO surfaces and energy gap for **(3)**.

Table 5
The Physico-Chemical properties of (3) computed at (DFT/PBE0) and LANL2DZ level of theory.

Parameters	Values
HOMO (ev)	−5.20
LUMO (ev)	−4.94
Energy gap (△E) (ev)	0.26
Ionization potential (IP) (ev)	5.20
Electron affinity (EA)	4.94
Electrophilicity Index (ω)	98.86
Chemical Potential (μ) (D)	−5.07
Electro negativity (χ) (ev)	5.07
Softness (*S*) (ev)	3.84
Hardness (η) (ev)	0.13

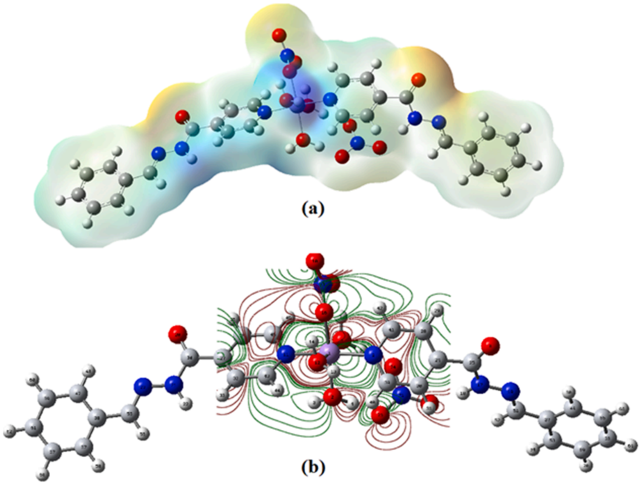

Fig. 15. (a) Molecular Electrostatic Potential (MEP) 3D Surface. (b) 2D contour plot (down) calculated at DFT/PBEPBE and LANL2DZ basis sets.

that hydrogen bonding and steric interactions play an important role in the interactions of **(2)** and **(3)** with 2X22 (Table 7).

4. Conclusion

A new complex model Mn-based [Mn $(L)_2(H_2O)_3(NO_3)_2$] was synthesized and characterized by single crystal X-ray diffraction. The crystal structure of **(3)** is governed by conventional O/N—H ···O H-bonding and non-conventional C—H ···O intermolecular interactions. Further, the 3D hydrogen bonds network of **(3)** presents supramolecular hetero and homo-synthons which play an important role in shaping this supramolecular complex. In **(3)** the organic entity behaves as two monodentate ligands and the metal center adopts a distorted octahedral coordination. Furthermore, the molecular arrangement of organic entities shows an alternating of two cationic layers parallel to the [1 0 4] and [1 2 4] plans. Moreover, an attractive combination of weak forces, viz. π–π stacking and $N_{\text{lone-pair}}$…C—H interactions established between organic ribbons layers, contributes to the final solid-state architecture. Additionally, the Hirshfeld surfaces analysis and associated fingerprint plots were used to explore and quantify the relative proportions of intermolecular non-covalent interactions within the complex. In this present investigation, the O···H contacts are the most responsible for building the supramolecular organisation with respect to their contribution to the overall stability of the crystal packing.

The physico-chemical properties of **(3)** were characterized by NMR, IR and UV–vis spectroscopy. The electrochemical behaviour of manganese (II) isonicotinic acid benzylidene-hydrazide complex was studied using cyclic and square wave voltammetry. The values of the electrochemical parameters characteristic of the voltammogram corresponding to the oxidation of Mn (II) to Mn (III) complex revealed a diffusion-controlled behaviour. DFT-optimized molecular geometry of Mn complex was performed by the (DFT/PBE0) and LANL2DZ method. The results showed good correlation with the experimental data. In addition, from the docking results, it has been understood that steric interactions and hydrogen bonds played an important role in the interaction between the molecules and the active site of 2X22 enzyme. The remarkable activity of (3) may be due to the fact that it contains both OH and H_2O units, which may play a crucial role in biological activities.

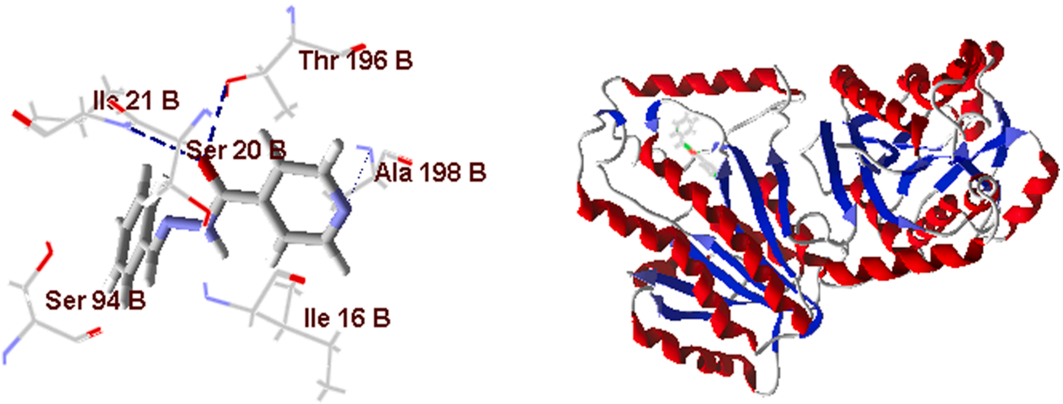

Fig. 16. The best score docking solution of **(2)** at the binding site of 2X22 (blue lines represent the hydrogen bonds and the amino acid residues in the binding pockets are indicated as gray). (For interpretation of the references to colour in this figure legend, the reader is referred to the web version of this article.)

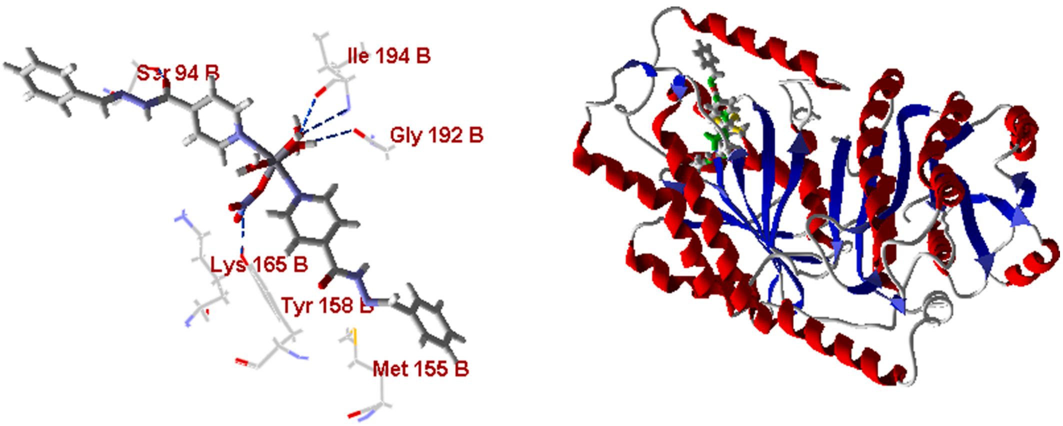

Fig. 17. The best score docking solution of **(3)** at the binding site of 2X22 (blue lines represent the hydrogen bonds and the amino acid residues in the binding pockets are indicated as gray). (For interpretation of the references to colour in this figure legend, the reader is referred to the web version of this article.)

Table 6
Mulliken charge distribution of metal, organic atoms and water in **(3)**.

Atoms	DFT	Atoms	DFT
Mn	0.465275	15N	0.185536
2O	−0.684190	16O	−0.324361
3H, 4H (H_2O)	0.408984 0.401693	17N	−0.399530
5O	−0.683251	18H	0.365663
6H, 7H (H_2O)	0.426149 0.423476	19N	0.032998
8O	−0.212894	20O	−0.218205
9N	−0.194855	21N	−0.413132
10O	−0.165612	22H	0.282724
11N	−0.223064	23N	0.060438
12O	−0.645540	24C	0.297462
H13, H14 (H_2O)	0.425942 0.450536	26O	−0.294719

CRediT Authorship contribution statement

Ali Akram Derardja: Synthesis. **Lynda Golea:** Spectroscopic characterizations, Voltammetry, Molecular docking, DFT calculations, Methodology, Visualization, Writing-original draft. **Rim Benali-Cherif:** Writing, Crystal structure description, Hirshfeld surface analysis, Reviewing, Validation. **Dominique Luneau:** X-ray diffraction on single crystals, Structural refinement, Validation, Reviewing. **Zina Boutobba:** Visualization, Software. **Youcef Boumedjane:** DFT calculations. **Hassina Harkat:** Investigation, Supervision.

Table 7
Binding interactions details of **(2)** and **(3)** docked at the binding pocket of the target proteins 2X22.

Ligand	Enzyme	Type of interaction	Residue	H Bond kcal/mol
(2)	PDB: 2X22	- Hydrogen bond - Steric interactions	- lle B 21, thy B 196 - ala B 198, ser B 20, ser B 94, lle B 16	−1.61
(3)	PDB: 2X22	- Hydrogen bond - Steric interactions	- gly B 192, lle B 194, try B 158, ser B 94 - met B 155, ser B 94, try B155, try B 165	−7.25

Declaration of Competing Interest

The authors declare that they have no known competing financial interests or personal relationships that could have appeared to influence the work reported in this paper.

Data availability

No data was used for the research described in the article.

Acknowledgement

We are grateful to Prof. Abdecharif Boumaza and Prof. Abdelkader

Djelloul from Laboratoire des Structures, Propriétés et Interactions Inter Atomiques (LASPI2A), Abbe Laghrour Khenchela University for the FT–IR IR and UV–vis measurements. And we thank all the people who helped to carry out this work such as ^{1}H NMR, ^{13}C NMR and Cyclic voltammetry. We also thank the Algerian MESRS (Ministère de l'Enseignement Supérieur et de la Recherche Scientifique) and DGRSDT (Direction Générale de la Recherche Scientifique et du Développement Technologique) and Abbes Laghrour Khenchela University, for financial support.

Appendix

The crystallographic data for the title compound **(3)** reported in this work is deposited at the Cambridge Crystallographic Data Center under CCDC N°. 2133366. These data may be available through the Cambridge Crystallographic Data Centre, 12 Union Road, Cambridge CB2 1EZ, UK; fax: (+44) 1223–336-033; email via. ku.ca.mac.cdcc@tisoped.

Appendix A. Supplementary material

Supplementary data to this article can be found online at https://doi.org/10.1016/j.inoche.2022.110198.

References

[1] B. Miroslaw, Homo- and hetero-oligonuclear complexes of platinum group metals (PGM) coordinated by imine Schiff base ligands, Int. J. Mol. Sci. 21 (10) (2020) 3493.

[2] M. Sayed Alam, J.H. Choi, D.U. Lee, Synthesis of novel Schiff base analogues of 4-amino-1,5-dimethyl-2-phenylpyrazol-3-one and their evaluation for antioxidant and anti-inflammatory activity, Bioorg. Med. Chem. 20 (13) (2012) 4103–4111.

[3] A.M. Vijesh, A.M. Isloor, P. Shetty, S. Sudarshan, H.K. Fun, New pyrazole derivatives containing 1,2,4-triazoles and benzoxazoles as potent antimicrobial and analgesic agents, Eur. J. Med. Chem. 62 (2013) 410–415.

[4] M. Sedighipoor, A.H. Kianfar, W.A.K. Mahmood, M.H. Azarian, Synthesis and electronic structure of novel Schiff bases Ni/Cu (II) complexes: evaluation of DNA/serum protein binding by spectroscopic studies, Polyhedron 129 (2017) 1–8.

[5] M. Arif, M.M.R. Qurashi, M.A. Shad, Metal-based antibacterial agents: synthesis, characterization, and in vitro biological evaluation of cefixime-derived Schiff bases and their complexes with Zn(II), Cu(II), Ni(II), and Co(II), J. Coord. Chem. 64 (11) (2011) 1914–1930.

[6] M.N. Uddin, S.S. Ahmed, S.M. Rahatul Alam, Biomedical applications of Schiff base metal complexes, Coord. Chem. Rev. 73 (2020) 3109–3149.

[7] A. Dzeikala, A. Sykula, Schiff bases as important class of pharmacological agents, J. Pharm. Pharmacol. 6 (2018) 989–1009.

[8] Z. Hussain, E. Yousif, A. Ahmed, A. Altaie, Synthesis and characterization of Schiff's bases of sulfamethoxazole, Org. Med. Chem. Lett. 4 (1) (2014) 1–4.

[9] E. Yousif, N. Salih, J. Salimon, Improvement of the photostabilization of PVC films in the presence of 2N-salicylidene-5-(substituted)-1,3,4-thiadiazole, J. Appl. Polym. Sci. 120 (2011) 2207–2214.

[10] E. Yousif, A. Ahmed, M. Mahmoud. New Organic Photostabilizers for Rigid PVC Against Photodegradation, Lambert Academic, Saarbrücken, 2012.

[11] S.D. Joshi, S.R. Dixit, S. Gadag, V.H. Kulkarni, T.M. Aminabhavi, Molecular docking, synthesis, and antimycobacterial activities of pyrrolyl hydrazones and their copper complexes, Res. Rep. Med. Chem. 6 (2016) 1–14.

[12] Z.H. Chohan, M. Arif, Z. Shafiq, M. Yaqub, C.T. Supuran, In vitro antibacterial, antifungal & cytotoxic activity of some isonicotinoylhydrazide Schiff's bases and their cobalt (II), copper (II), nickel (II) and zinc (II) complexes, J. Enzym. Inhib. Med. Chem. 21 (1) (2006) 95–103.

[13] M.J. Hearn, M.H. Cynamon, M.F. Chen, R. Coppins, J. Davis, H. Joo-On Kang, A. Noble, B. Tu-Sekine, M.S. Terrot, D. Trombino, Preparation and antitubercular activities in vitro and in vivo of novel Schiff bases of isoniazid, Eur. J. Med. Chem. 44 (10) (2009) 4169–4178.

[14] M. Iqbal, M.A. Bhat, F. Shakeel, Development and validation of UHPLC-MS/MS assay for rapid determination of a carvone Schiff base of isoniazid (CSB-INH) in rat plasma: application to pharmacokinetic study, Biomed. Chromatogr. 29 (2015) 876–882.

[15] S.M.S.V. Wardell, M.V.N. de Souza, J.L. Wardell, J.N. Low, C. Glidewell, Supramolecular structures in N-isonicotinoyl arylaldehydehydrazones: multiple hydrogen-bonding modes in series of geometric isomers, Acta Cryst. B 63 (2007) 879–895.

[16] G.M. Sheldrick, SHELXT - Integrated space-group and crystal-structure determination, Acta Cryst. A 71 (2015) 3–8.

[17] G.M. Sheldrick, Crystal structure refinement with SHELXL, Acta Cryst. C 71 (2015) 3–8.

[18] O.V. Dolomanov, L.J. Bourhis, R.J. Gildea, J.A.K. Howard, H. Puschmann, OLEX2: a complete structure solution, refinement and analysis program, J. Appl. Cryst. 42 (2009) 339–341.

[19] C.F. Macrae, I. Sovago, S.J. Cottrell, P.T.A. Galek, P. McCabe, E. Pidcock, M. Platings, G.P. Shields, J.S. Stevens, M. Towler, P.A. Wood, Mercury 4.0: from visualization to analysis, design and prediction, J. Appl. Cryst. 53 (2020) 226–235.

[20] H. Blessing, An empirical correction for absorption anisotropy, Acta Cryst. A 51 (1995) 33–38.

[21] S.K. Wolff, D.J. Grimwood, J.J. McKinnon, M.J. Turner, D. Jayatilaka, M. A. Spackman. CrystalExplorer, Version 3.1, University of Western Australia, Perth, 2012.

[22] R.D. Dennington, T.A. Keith, J.M. Millam, GaussView 5.0.8, Gaussian Inc, 2008.

[23] K.K. Sharma, R. Singh, N. Fahmi, R.V. Singh, Synthesis, coordination behavior, and investigations of pharmacological effects of some transition metal complexes with isoniazid Schiff bases, J. Coord. Chem. 63 (2010) 3071–3082.

[24] P.J. Hay, W.R. Wadt, Ab initio effective core potentials for molecular calculations. Potentials for K to Au including the outermost core orbitals, J. Chem. Phys. 82 (1) (1985) 299–310.

[25] P. Pulay, F. Torok, Acta Chim. Acad. Sci. Hung. 47 (1965) 273.

[26] G. Keresztury, G. Jalsovszky, An alternative calculation of the vibrational potential energy distribution, J. Mol. Struct. 10 (1971) 304–305.

[27] D. Sharma, A. Radha, S. Kumar, A.K. Jassal, N. Rani, Vikas, S.K. Pandey, Synthesis, single crystal X-ray, DFT and HSA of N-donor stabilized complexes of cobalt (II) diphenyldithiophosphate: an experimental and theoretical approach, J. Mol. Struct. 1207 (2020) 127835.

[28] A.B. Bocasly, Cyclic voltammetry, electrochemical technique. Characterization of Materials, second ed., Wiley, 2012.

[29] T. Scior, I. Meneses Morales, S.J. Garcés Eisele, D. Domeyer, S. Laufer, Antitubercular isoniazid and drug resistance of *Mycobacterium tuberculosis*–a review, Arch. Pharm. (Weinheim) 335 (2002) 511–525.

[30] P. Maity, T. Mahapatra, R. Kumar Ghosh, R.M. Gomila, A. Frontera, A. Ghosh, Synthesis of Ni(II)–Mn(II) complexes using a new mononuclear Ni(ii) complex of an unsymmetrical N2O3 donor ligand: structures, magnetic properties and catalytic oxidase activity, Dalton Trans. 50 (13) (2021) 4686–4699.

[31] J. Bernstein, R.E. Davis, L. Shimoni, N.L. Chang, Patterns in hydrogen bonding: functionality and graph set analysis in crystals, Angew. Chem. Int. Ed. Engl. 34 (1995) 1555–1573.

[32] K.A. Siddiqui, C-H···Onitrate synthon assisted molecular assembly of hydrogen bonded Ni (II) and Cu (II) complexes, J. Coord. Chem. 66 (12) (2013) 2039–2050.

[33] M.A. Spackman, J.J. McKinnon, Fingerprinting intermolecular interactions in molecular crystals, CrystEngComm. 4 (66) (2002) 378–392.

[34] R. Benali-Cherif, R. Takouachet, W. Falek, N. Benali-Cherif, C. Jelsch, H. Merazig, M. Hafied, E.-E. Bendeif, N. Bouslah Mokhnachi, K. Taibi, Synthesis, structural elucidation, spectroscopic, Hirshfeld surface analysis and theoretical simulation of a new adeninium orthoperiodate (1-) bis(hydrate) organic–inorganic hybrid crystals, J. Mol. Struct. 1224 (2021), 129034.

[35] R. Takouachet, R. Benali-Cherif, E.E. Bendeif, C. Jelsch, F. Yahia Cherif, A. Rahmouni, N. Benali-Cherif, The supramolecular behavior and molecular recognition of adeninium cations on anionic hydrogen selenite/diselenite frameworks: a structural and theoretical analysis, J. Mol. Struct. 1229 (2021), 129836.

[36] W.M. Eldehna, M. Fares, M.M. Abdel-Aziz, H.A. Abdel-Aziz, Design, synthesis and antitubercular activity of certain nicotinic acid hydrazides, Molecules. 20 (5) (2015) 8800–8815.

[37] M.L. Dianu, A. Kriza, N. Stanica A.M. Musuc, Transition metal M (II) complexes with isonicotinic acid 2-(9-anthrylmethylene) -hydrazide, J. Serb. Chem. Soc. 75 (2010) 1515–1531.

[38] P. Suneetha, C.S. Karigar, N.H Manjnath, K.N. Mahendra, Cobalt (II), Ni (II), Cu (II), Zn (II), CD (II), Hg (II), U0 (2) (VI) and th (IV) complexes from ONNN Schiff base ligand, J. Chilean Chem. Soc. 53 (4) (2008) 1653–1657.

[39] A.M. Shaker, L.A.E. Nassr, M.S.S. Adam, I.M.A. Mohamed, Hydrophilicity and acid hydrolysis of water-soluble antibacterial iron(II) Schiff base complexes in binary aqueous solvents, Russ. J. Gen. Chem. 83 (2013) 2460–2464.

[40] A. Choudhury, B. Geetha, N.R. Sangeetha, V. Kavita, V. Susila, S. Pal, Synthesis, structure and properties of manganese (II) complexes with Aroylhydrazones of 2-pyridine-carboxaldehyde, J. Coord. Chem. 48 (1999) 87–95.

[41] B.M. Sarhan, A.H. Abed, R.M. Rumez, Synthesis and characterization of some mixed ligand complexes of quinaldic acid and α-picoline with some metal salts, AL-Mustansiriyah J. Sci. 24 (4) (2013) 65–74.

[42] U. Sivagnanam, M. Palaniandavar, Influence of chelatering size and number of sulfur-donor atoms on spectra and redox behaviour of copper (II) bis (benzimidazolyl)tetra- and penta-thloether complexes, J. Chem. Soc. Dalton Trans. 15 (1994) 2277–2283.

[43] J.N. Bavane, R.B. Mohod, Synthesis, characterization and electrochemical studies of symmetrical Schiff base complexes of [1-(5 chloro-2-hydroxy-4-methyl- phenyl) ethanone-4-chloro (-3-trifluro methyl) aniline], J. Pharm. Innov. 7 (2018) 149–152.

[44] S. Karastogianni, S. Girousi, Electrochemical behavior and voltammetric determination of a manganese (II) complex at a carbon paste electrode, Anal. Chem. Insights. 11 (11) (2016) 1–11.

[45] S. Karastogianni, S. Girousi, Electrochemical Behavior and Voltammetric Determination of a Manganese (II) Complex at a Carbon Paste Electrode, Anal. Chem. Insights 11 (2016) 1–11.